coatings

MDPI

Article

Experimental Research on Collapsibility of Xi'an Loess Improved by Calcium Lignosulfonate

Zhentao Bai [1], Dongbo Li [1,2,*], Dong Zhao [1], Wei Lu [1,2,*] and Jiaping Liu [2]

[1] College of Science, Xi'an University of Architecture and Technology, Xi'an 710055, China
[2] State Key Laboratory of Green Building in Western China, Xi'an University of Architecture and Technology, Xi'an 710055, China
* Correspondence: ldb@xauat.edu.cn (D.L.); luwei@xauat.edu.cn (W.L.)

Abstract: To improve the problem of collapsibility of loess, adding industrial materials such as cement is common engineering treatment, but this seriously damages the reclamation performance of soil. Calcium lignosulfonate (CLS) from paper plant waste fluids is a natural bio-based polymer with good application prospects as a soil improver. In this paper, the collapsibility and mechanical properties of CLS improved loess were investigated using a collapsibility test, gray correlation analysis, and an unconfined compressive strength test (UCS). In addition, the strengthening mechanism of CLS-improved loess was also explored based on scanning electron microscopy (SEM), microstructure parameters, and X-ray diffraction. The collapsibility coefficient decreased rapidly after CLS was admixed, and the single and double-oedometer methods showed the same change trend. The order of grey correlation degree of collapsibility on each index from large to small was: moisture content, pore ratio, dry density, and CLS content. The dosage of CLS greatly influenced the mechanical properties and collapsibility of stabilized loess. The optimum amount of CLS for Xi'an loess was 3%, at which the collapsibility coefficient was reduced by more than 95%, and the 28 d UCS increased by 180.01%. From the microstructure and mineral composition analysis perspective, CLS plays a role in filling pores and linking soil particles. After the protonation and ion exchange effect of CLS, the grain size and double electric layer thickness of mineral composition were reduced, and the structural compactness was increased. These research results are of great scientific significance for the ecological modification of soils.

Keywords: loess; calcium lignosulfonate; collapsibility; grey correlation analysis; unconfined compression strength; microstructure; strengthening mechanism

check for updates

Citation: Bai, Z.; Li, D.; Zhao, D.; Lu, W.; Liu, J. Experimental Research on Collapsibility of Xi'an Loess Improved by Calcium Lignosulfonate. *Coatings* **2023**, *13*, 157. https://doi.org/10.3390/coatings13010157

Academic Editor: Manuel Miguel Jordan-Vidal

Received: 18 December 2022
Revised: 7 January 2023
Accepted: 9 January 2023
Published: 11 January 2023

Copyright: © 2023 by the authors. Licensee MDPI, Basel, Switzerland. This article is an open access article distributed under the terms and conditions of the Creative Commons Attribution (CC BY) license (https://creativecommons.org/licenses/by/4.0/).

1. Introduction

Loess is widely distributed in China's central and western regions, covering more than 6% of the area [1]. It is mainly composed of quartz, clay minerals, and dissolved salts. The unique skeleton particle connection method leads to poor properties such as multiple pores and high compression [2]. Under the erosion and infiltration of rainwater, the salts in the loess are easily dissolved, resulting in the rearrangement of soil particles and collapsibility, which often causes geological hazards such as landslides and foundation instability [3].

For the evaluation of engineering collapsibility in loess areas, the method of combining the results of indoor tests and in-situ tests (field static load test, field immersed water test) has often been used. Researchers have conducted a lot of research to address the problem of loess collapsibility. For instance, physical methods include strong tamping, replacement filling and adding plant fibers to reduce collapsibility, but durability is usually poor [4,5]. Mixing cement and other industrial materials makes the soil highly alkaline, which, together with heavy metal ions in these materials, causes severe damage to the surrounding environment and prevents soil reclamation [6]. In addition, in recent years, scholars have used nanomaterials and polymer materials to improve loess. Although these

can somewhat inhibit loess's ability to collapse, their high price prevents industrialization and widespread use. [7]. Therefore, research into economical and environmentally friendly soil improvement materials has become an essential issue in solving the problem of loess collapsibility.

Industrial lignin mainly comes from paper mill waste liquor and biofuel by-products. China's paper industry produces about 0.5 billion tons of industrial lignin annually. As a derivative of lignin, calcium lignosulfonate (CLS) contains various active functional groups and has good cohesiveness, chelating and anti-corrosive properties [8]. However, more than 95% of industrial lignin is discharged into rivers in wastewater or directly concentrated and incinerated every year. If industrial lignin is utilized for loess treatment, it can solve the waste pollution problem and achieve large-scale ecological modification [9].

Improving the mechanical properties and durability of untreated soils has been the main focus of research on CLS-improved soils. Zhang et al. [10] used CLS to treat silts. The results of unconfined compressive strength (UCS) and California bearing ratio tests showed that CLS could effectively improve the particle gradation and mechanical properties of silts. Yang et al. [11] investigated the durability of CLS-improved soils by a water immersion disintegration test and a freeze-thaw cycle test. They concluded that the water stability and freeze-thaw durability of CLS-improved soils were significantly than in untreated soils. Ceylan et al. [12] used CLS to treat low-plasticity clay in Iowa. The results showed that CLS could effectively improve the engineering properties of the soil and the treatment has been successfully applied to the curing and dust treatment of low-grade traffic roadbeds and pavements.

Currently, research on the improvement of loess is still in its initial stage. Wang et al. [13] found that CLS can improve the cyclic shear deformation and liquefaction resistance of loess by dynamic triaxial tests for the structural characteristics of loess. He et al. [14] found that the permeability of CLS was significantly reduced when mixed into loess, and could improve the engineering properties of loess. Hou et al. [15] studied the modification of loess in the Lanzhou area and concluded that CLS could react with clay minerals in loess to produce quartzite and carbonate minerals, which made the soil structure denser.

At present, CLS-improved loess is mainly used to improve mechanical properties and durability, but there are fewer reports on addressing the collapsibility of loess. In addition, because of the complex characteristics of CLS, the strengthening mechanism of CLS-improved loess is not as clear as that of traditional stabilizers such as cement, and research on the intrinsic connection between microstructure and macroscopic properties after CLS modification is quite limited. As a result, CLS was chosen as the material in this study to estimate the collapsibility coefficient and the mechanical characteristics of CLS-improved loess. The correlation between the major physical indices and the collapsibility coefficient were investigated. Scanning electron microscopy tests (SEM), microstructural parameters, and X-ray diffraction tests (XRD) were used to analyze microstructure and mineral composition changes before and after CLS modification and to explore the intrinsic mechanism of CLS-improved loess collapsibility. We combined our experimental results with existing studies to elucidate the potential to overcome the collapsibility of loess. The results provide a reference for the construction of highway roadbeds in loess-collapsible areas.

2. Materials and Test Methods

2.1. Materials

Soil samples were extracted from a highway project site in Xi'an, Shaanxi, China, at a depth of 3–4 m. The soil was crushed, air-dried, and passed through a 2 mm sieve. The basic physical properties of the loess were determined according to the ASTM D4318 standard [16], as shown in Table 1. Proctor compaction tests were used to measure optimum moisture content and maximum dry density as 18.0% and 1.69 g/cm^3, respectively.

Table 1. Fundamental physical indexes of tested loess.

Property	Value
Natural water content/%	2.87
Natural density/(g·cm^{-3})	1.17
Liquid limit/%	47.2
Plastic limit/%	35.5
Plasticity index	11.8
Specific gravity	2.70
Clay (<0.002 mm)	19.56
Silt (0.002–0.074 mm)	79.21
Sand (0.074–2 mm)	1.23
Maximum dry density/(g·cm^{-3})	1.69
Optimum moisture content/%	18.0

The CLS utilized in this investigation (Figure 1) was produced by Shanghai McLean Biochemical Technology Co., Ltd., Shanghai, China. It was a solid brownish powder with a specific viscosity and fragrant odor that was readily soluble in water. Table 2 and Figure 2 show the main components and microscopic morphology of CLS, respectively.



Figure 1. Calcium lignosulfonate (CLS) used in the test.

Table 2. Composition of CLS in the test.

Molecular Formula	Molecular Weight	Lignin Content/%	Moisture/%	Carbon Content/%	Sulfur Content/%	pH
$C_{20}H_{24}CaO_{10}S_2$	528.61	≥96	5	40	5	7.00

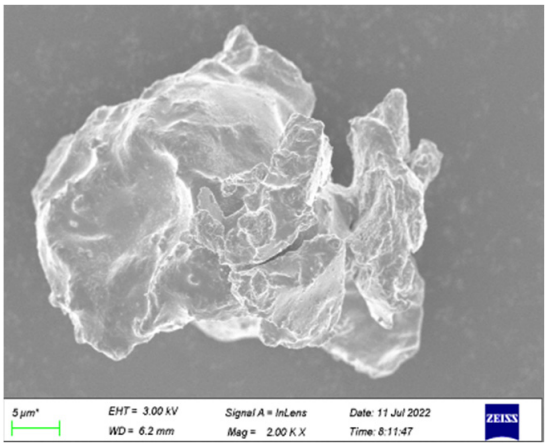

Figure 2. Microstructure of CLS.

2.2. Sample Preparation

The collected natural soil was air-dried and broken down by crushing with a rubber hammer. The samples were passed through a 2 mm sieve to remove any oversized particles in the experiment. Different amounts of CLS (0%, 1%, 3%, 5%, 7%) were mixed directly into the loess; the noted quantity being the ratio of the modifier to the mass of dry soil. To ensure the uniform distribution of the modified additives, the mixtures were mixed manually for about 5 min after adding a measured amount of distilled water, and the configured soil samples were placed in vinyl bags and sealed for 24 h. The resulting loess was then placed into a steel mold for the desired test and compacted by the static compaction method. The degree of compaction of the specimens prepared, according to ASTM D698, was 0.85 [17].

2.3. Testing Methods

2.3.1. Collapsibility Test

The collapsibility test was performed with a WG single-lever consolidation instrument produced by Nanjing Soil Instrument Factory (Nanjing, China). The test procedure is shown in Figure 3. The test process was carried out in accordance with the provisions of the collapsibility test in GB 50025-2018 [18]. The size of the cutting ring used for the specimens was Φ79.8 mm × 20 mm. The improved loess samples used for the tests had optimum moisture content. The collapsibility characteristics of CLS-improved loess were analyzed using single and double-oedometer methods.

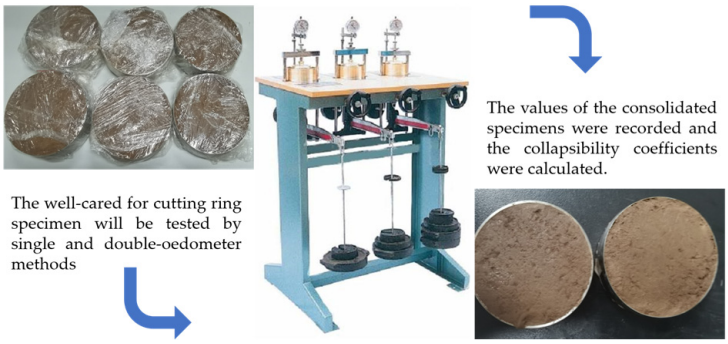

Figure 3. Block diagram of collapsibility test.

2.3.2. UCS Test

To evaluate the strength improvement effect of the stabilizer, the unconfined compressive strength test was conducted according to ASTM D4219-02 [19]. The test was performed using a YYW-II electric calcareous soil unconfined pressure instrument manufactured by Nanjing Soil Instrument Factory with a 3 mm/min loading rate. Soil samples with different CLS contents (0%, 1%, 3%, 5% and 7%) were placed into a cylindrical mold 50 mm in diameter and 50 mm in height in three stages for static compaction. The resulting loess was cured in a standard curing chamber for specific times (1, 7, 14, 28 d). UCS tests were conducted on 20 groups of specimens, respectively.

2.3.3. SEM Test

SEM was conducted using an HITACHI SU8010 scanning electron microscope (HITACHI, Tokyo, Japan)for microstructure examination at a magnification of 1000 multiplication (Figure 4). The specimens were taken from the center of a 28 d UCS test block, prepared with a flake of approximately 1 cm^2 and a thickness of 2 mm. Before the test, the samples were freeze-vacuum dried to ensure complete sublimation of pore water in the specimens. In order to make the sample surface conductive and able to reflect secondary imaging, the prepared flake sample was sprayed with gold in an ion-sputtering device. The scanning electron microscope voltage was set to 20 kV. After a precise adjustment of focal length, the overall morphology of the sample was observed.

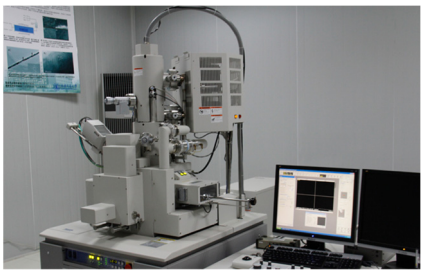

Figure 4. HITACHI SU8010 scanning electron microscope.

2.3.4. XRD Test

The XRD test was performed using a D8 ADVANCE X-ray diffractometer from Bruker, Germany (Karlsruhe), to scan the untreated loess and 3% CLS-improved loess samples (Figure 5). The principle of this is shown in Figure 6. The samples were in the form of powder, had no apparent granularity, and had been ground and put through a 200-mesh filter. The basic parameters of the diffractometer were a Cu target, a power of 3 kW, and wavelength λ = 1.54056 Å. The scanning speed was 2°/min, and the scanning range was between 5° and 90°.



Figure 5. D8 ADVANCE X-ray diffractometer.

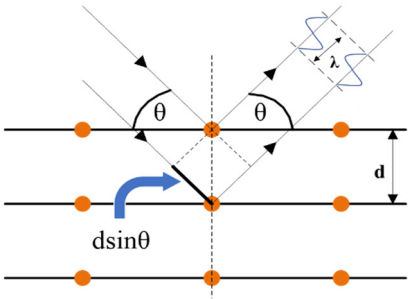

Figure 6. X-ray diffraction principle, where d is the crystal plane spacing, θ is the angle of incidence, and λ is the wavelength of the beam.

3. Results and Discussion

3.1. Collapsibility Characteristics of Improved Loess

The collapsibility coefficient is the ratio of the height difference between the soil before and after water immersion and the initial height of the soil under particular pressure, which is one of the critical mechanical parameters to evaluate the collapsibility of loess. It is expressed by the following equation [18]:

$$\delta_s = \frac{h_p - h_{pb}}{h_0} = \frac{e_{pb} - e_p}{1 + e_0} \quad (1)$$

where h_p is added to a certain pressure related to the height after sinking and stabilization (mm), h_{pb} is the specimen under the action of water immersion related to the height after sinking and stabilization (mm), h_0 is the initial height of the sample (mm), e_{pb} is the pore ratio of the saturated specimen at a specific pressure, e_p is the pore ratio of the original moisture content specimen at a particular pressure, and e_0 is the initial pore ratio.

According to Equation (1), the collapsibility coefficient of improved loess under different pressures and admixtures is derived using the single and double-oedometer methods, respectively, as shown in Figure 7. As can be seen from the figure, the collapsibility coefficients measured by the two methods showed the same trend of change. That is, at a pressure of 50 kPa, the CLS-improved loess with different contents showed strong collapsibility. With increasing pressure, the collapsibility decreased significantly, and the collapsibility coefficient showed a trend of rapid decrease and then stabilization. Under the pressure condition of 400 kPa, the collapsibility coefficient of the improved loess with different CLS contents dropped to below 0.015, and behaved like non-collapsible loess.

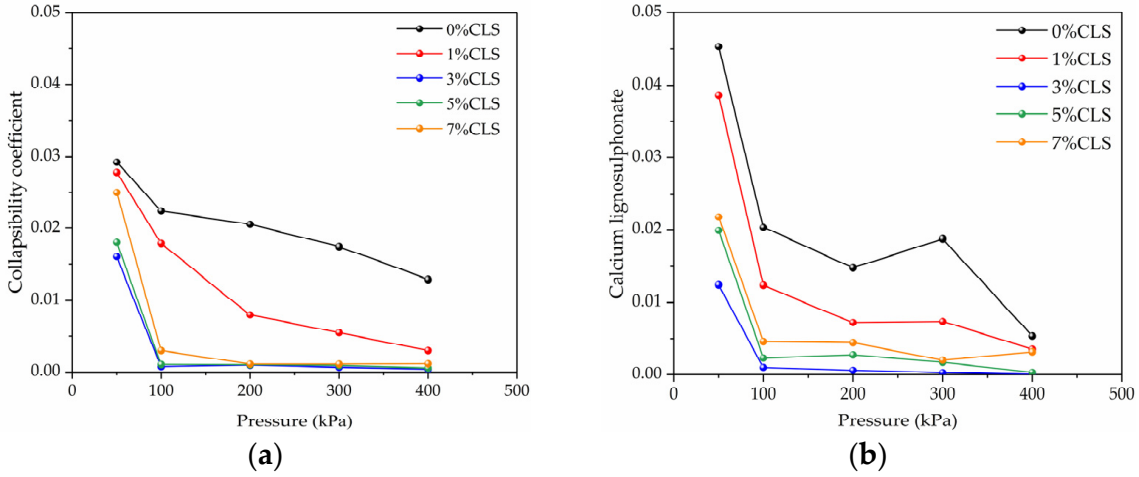

Figure 7. Collapsibility coefficient of improved loess with different compositions under various pressures. (**a**) single-oedometer method; (**b**) double-oedometer method.

It can be seen from Figure 7 that the collapsibility coefficients obtained by the double-oedometer method were generally higher than those by the single-oedometer method due to the different orders of immersion and loading resulting in different results in the collapsibility process. The single-oedometer method was loaded and compressed first. The improved loess tended to be dense and less porous. During saturation with water, it is difficult for water to enter the soil particles, and the collapsibility process is insufficient [20]. The double-oedometer method loads the improved loess sample when fully immersed in water, similar to the compression process of saturated soil. Due to the long immersion time, the salts and cementing substances in the CLS-improved loess dissolve in water. The collapsibility process proceeds to a greater extent, resulting in a significantly higher collapsibility coefficient [21].

As seen from the collapsibility test, the collapsibility of the improved loess was reduced significantly with the incorporation of CLS. To further analyze the collapsibility of improved loess related to primary physical indices under standard pressure, the collapsibility coefficients of improved loess with differing moisture content (ω), dry density (ρ_d), pore ratio (e) and CLS content (θ) under 200 kPa pressure were estimated, and are plotted in Figure 8.

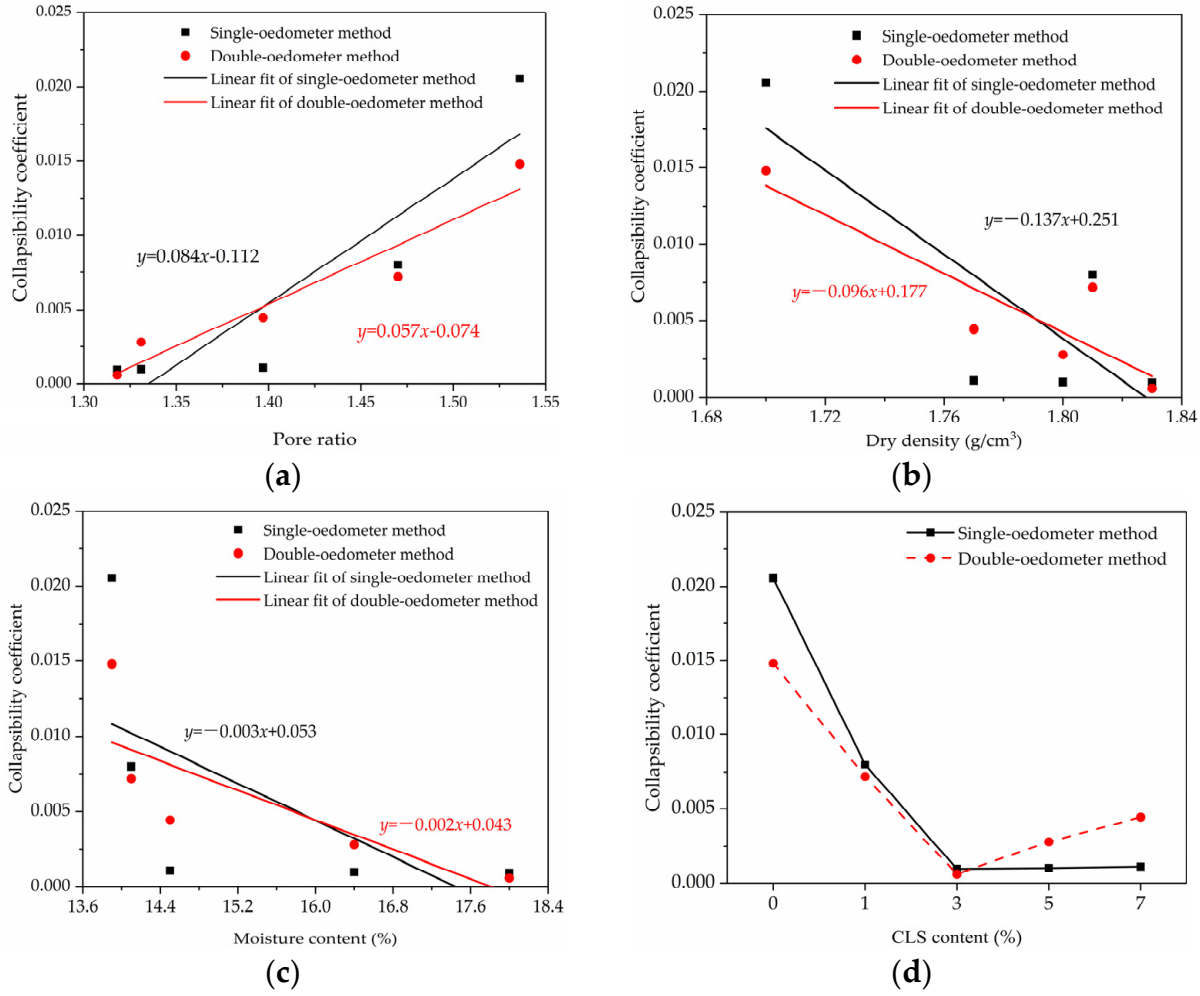

Figure 8. Relation between collapsibility coefficient and physical indexes at 200 kPa. (**a**) Pore ratio; (**b**) dry density; (**c**) moisture content; (**d**) CLS content.

As can be seen from the figure, the test results of single and double-oedometer methods were consistent. The collapsibility coefficient was positively correlated with the pore ratio, and negatively correlated with dry density and moisture content.

There was no linear correlation between the content of CLS and the collapsibility coefficient, and the improvement effect was optimal when 3% CLS is added. In the single-oedometer method test, the collapsibility coefficient was reduced from 0.0206 in untreated loess to 0.0009 at a 3% CLS content, a reduction of 95.63%. In the double-oedometer test, the collapsibility coefficient decreased from 0.0148 in the untreated loess to 0.0006 with 3% CLS doping, a decrease of 95.95%. With further increase of CLS dosing, the collapsibility coefficient rebounded slightly, but it was still much lower than in untreated loess.

It can be seen that the addition of CLS can effectively inhibit the intrusion of water because CLS contains a large number of lipophilic groups, such as phenyl propane groups, that have a significant repulsive effect on water molecules [22]. In addition, CLS can fill pores and connect soil particles to form a denser agglomerate, which can effectively reduce the permeability and dispersion of the improved loess.

3.2. Grey Relational Analysis of Collapsibility

From the results above, it is clear that the collapsibility of loess is influenced by a combination of factors [23]. However, inconsistencies in the units of measurement and orders of magnitude of the parameters make it difficult to analyze the pattern of influence of the physical indicators on the collapsibility factor.

Gray system theory is an effective method for researching incomplete information systems [24]. Gray correlation analysis is the core element of gray system theory, an analytical technique used to characterize the degree of contribution of each influencing factor on the main behavior. Relational degree (γ_i) is the main parameter to describe the interrelationship between system elements. A larger γ_i indicates a stronger dependence of the parent sequence on specific sub-sequences and the closeness of the relationship between them [25].

A gray correlation analysis was performed on the collapsibility of loess after CLS improvement (Figure 9 shows the flow chart). First, the parent sequence (δ_s) and sub-sequences (ρ_d, e, θ, ω) were determined, then the range variation method was applied to eliminate the influence between the dimensions of each sequence, and the extremes (Δ_{max} and Δ_{min}) were selected in the new sequence formed Δ_{ij}. Finally, the correlation coefficient matrix $\boldsymbol{L}$ and the relational degree γ_i were calculated and ranked for analysis.

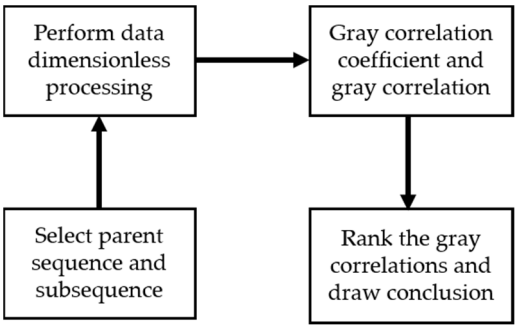

Figure 9. Flow chart of grey correlation analysis.

Each factor in the correlation coefficient matrix $\boldsymbol{L}$ was calculated using the following equation [26]:

$$l_{ij} = \frac{\rho\Delta_{max} + \Delta_{min}}{\rho\Delta_{max} + \Delta_{ij}} \quad (2)$$

where ρ is the resolution coefficient and $\rho \in (0,1)$ is usually taken as 0.5.

Due to the large and scattered data in the correlation coefficient, the analysis was not easy. Therefore, the correlation degree was defined as the average of the correlation coefficients and calculated using the following equation [27]:

$$\gamma_i = \frac{1}{n}\sum_{j=1}^{n} l_{ij} \quad (3)$$

Table 3 shows the gray correlation values derived from the two collapsibility methods at a standard pressure of 200 kPa. As seen from the table, the correlation rankings derived from the single and double-oedometer methods were consistent, and the order of the sensitive factors of improved loess collapsibility coefficient was moisture content, pore ratio, dry density, and CLS content, in that order.

Table 3. Grey correlation degree of physical indexes.

Physical Index	Single-Oedometer Method	Double-Oedometer Method
Moisture content ω	0.758	0.801
Pore ratio e	0.746	0.781
Dry density ρ_d	0.73	0.76
CLS content θ	0.588	0.557

Our correlation order differs from Wu et al.'s results [28]. This is attributed to the difference between the untreated loess and the improved loess. The gray correlations of

moisture content were 0.758 and 0.801, respectively, which rank first among the physical indicators. When the moisture content increases, there is not only strong combined water but also a certain amount of weak combined water between soil particles, which reduces the coulomb force and Van der Waals force between the particles and results in a decrease in cohesive forces on a macroscopic level. With the addition of CLS, the sensitivity of the soil to moisture content gradually increases, resulting in moisture content being the factor that most closely affects collapsibility [29]. Therefore, strict control of the water content of the CLS-improved soil is the key to preventing collapsibility.

The correlation between pore ratio and dry density on the collapsibility coefficient was similar, and was also the main factor affecting the collapsibility of CLS-improved soil. The collapsibility coefficient is negatively correlated with dry density and positively correlated with the pore ratio [30]. This means that when the dry density is larger, the pore ratio decreases, the soil structure is more compact, and external water cannot enter easily to increase collapsibility.

Although the direct correlation between CLS content and the collapsibility coefficient is low, the correlation shows significance when the gray correlation is greater than 0.3 [31]. With the incorporation of CLS, the maximum dry density of the improved loess increased, the optimum moisture content decreased, and the pore ratio decreased due to the filling of pores by CLS. The amount of CLS content indirectly affected the changes of each primary physical index and had a significant improvement effect on the loess collapsibility.

3.3. Unconfined Compressive Strength of Improved Loess

To further evaluate the curing effect of CLS-improved loess, UCS tests were conducted on improved loess with different CLS contents and curing ages.

As shown in Table 4 and Figure 10, at 1 d, the strength difference between improved loess with different CLS contents was not significant, and was comparable to the strength of untreated loess (80.77 kPa). With increasing curing age, the UCS difference was gradually more significant. The UCS of untreated loess at 1, 14, and 28 d were 80.77, 174.22, and 235.99 kPa, respectively, and the strength increases at 14 d and 28 d were 115.70% and 192.18%, respectively. The strength of the improved loess with 3% CLS content increased fastest, and its UCS at 1, 14, and 28 d were 126.70, 289.83, and 354.77 kPa, respectively; the strength increases at 14 d and 28 d reached 128.75% and 180.01%, respectively. The untreated loess and improved loess had the same growth trend with curing age, which means that the strength grew faster in the first 14 d and grew slowly with stability in the last 14 d [32]. This agrees with the results of previous related studies. Therefore, the curing age of the CLS-improved loess was found to be at least 14 d.

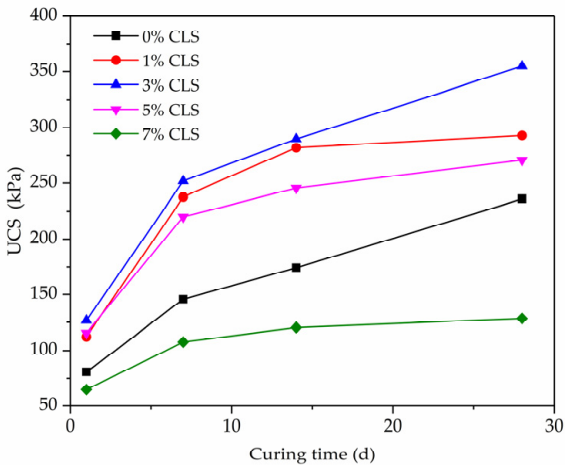

Figure 10. UCS of CLS improved loess.

Table 4. UCS of improved loess under different CLS content and curing age.

CLS Content (%)	UCS (kPa)			
	1 d	7 d	14 d	28 d
0	80.77	145.71	174.22	235.99
1	112.45	237.57	281.92	293.00
3	126.70	251.82	289.83	354.77
5	115.61	220.15	245.49	270.83
7	64.93	107.70	120.37	128.29

Figure 11 shows the curve of UCS with the content of CLS at 28 d curing age. As shown in the figure, the UCS of improved loess increases with the increase of the content of CLS and then decreases, and the maximum value is achieved when the content of CLS is 3%. When the content is too high, the strength of the improved loess declines. For instance, the UCS of the improved loess with 7% CLS content was only 54.36% of the untreated loess, since excess CLS preferentially forms agglomerates within the loess, and a large amount of CLS wraps around the soil particles, reducing the frictional resistance and skeletal strength between the soil particles [33]. Ceylan et al. [34] used two different industrial by-products of lignin to improve clay soils in Iowa, USA, and found that an excessive lignin admixture caused a loss of soil strength, which is consistent with the results of this paper. In addition, it can be seen that the relationship between UCS and the content of CLS is a quadratic polynomial. When the content of CLS was 2.88%, UCS had a maximum value.

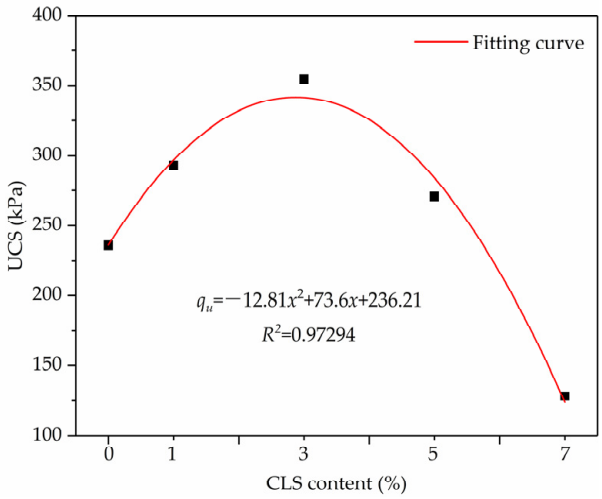

Figure 11. Curve of UCS with CLS content at 28 d curing age.

4. Analysis of the Strengthening Mechanism of Improved Loess

4.1. SEM Analysis

SEM tests were conducted on the improved loess to investigate microstructure and the strengthening mechanism of improved loess with different CLS content, as shown in Figure 12. As seen in Figure 12a, the untreated loess particles are angular and mainly show plate and granular shapes. The untreated loess is compacted but still contains many irregular aerial pores and intergranular pores. The structure is skeleton-like, and the soil particles are associated with each other by direct point contact and direct surface contact [35]. When subjected to water erosion and pressure, the soluble salt dissolves, the overhead structure is damaged, and the soil particles in direct contact with each other stagger and slip are accompanied by local fragmentation, eventually leading to structural reorganization.

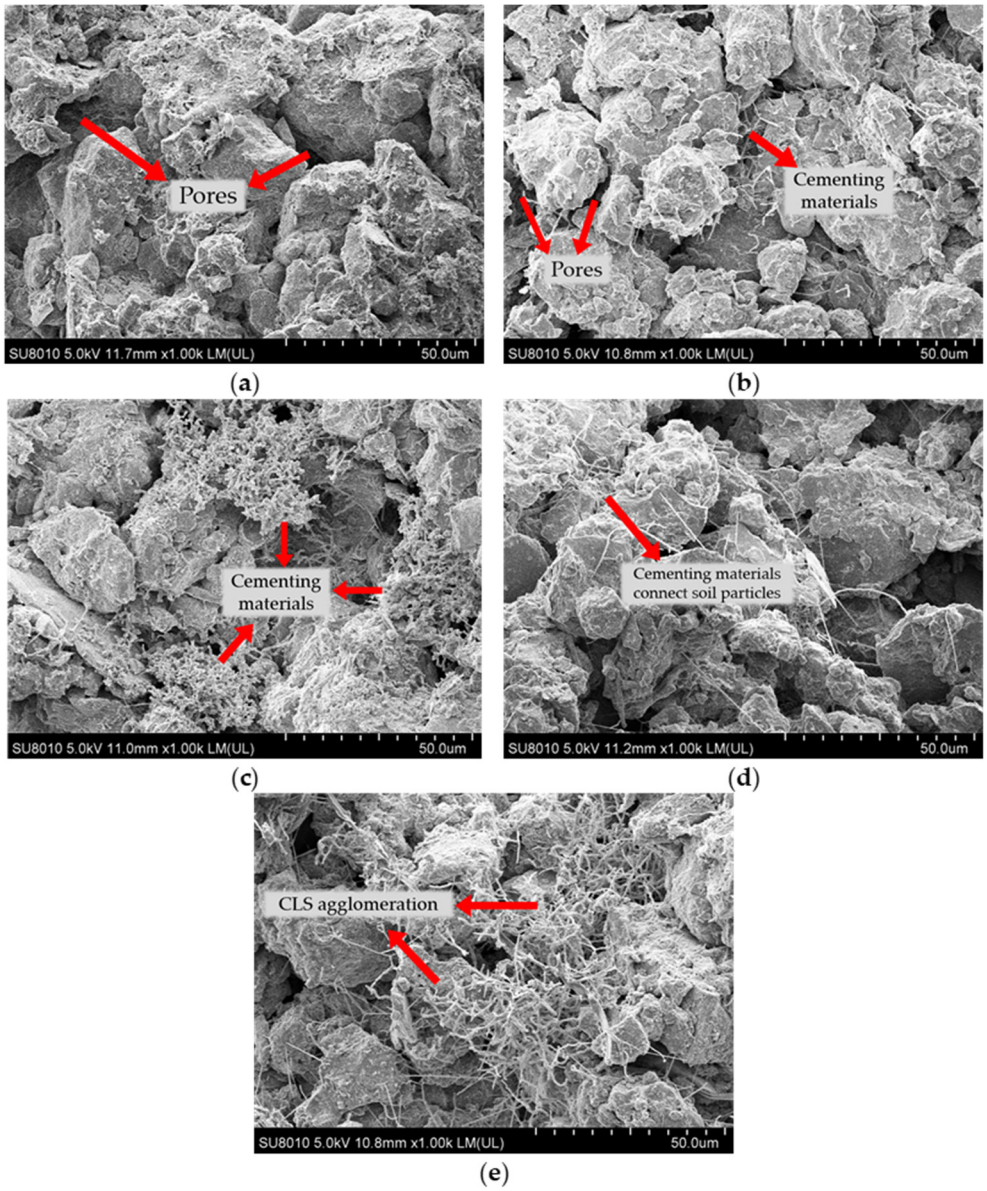

Figure 12. SEM of improved loess with different CLS content. (**a**) Untreated loess; (**b**) 1% CLS content; (**c**) 3% CLS content; (**d**) 5% CLS content; (**e**) 7% CLS content.

With the incorporation of CLS (Figure 12b–d), needle-like cementing materials began to develop, mainly concentrated in the particle connection and pores. A large number of aerial pores were filled with CLS, and the pore type was transformed into a closed type, which filled the pores and enhanced the cohesion between the soil particles [36].

On the other hand, the fibrous CLS types of cementing materials wrapped around the surface of soil particles, changing the soil particles from direct contact to indirect point contact and indirect surface contact linked by the cementing materials, thus increasing the effective contact area. Preliminary studies have shown that the flocculation-like structure through indirect contact has better load-bearing performance and water stability than the skeleton-like structure through direct contact [37].

However, when the content of CLS is too large (Figure 12e), it combines to form agglomerates. Although the number of pores is reduced, the increase in pore size makes some of the soil particles separate from each other. The cohesion of the improved loess increases at this time, but the internal friction between the soil particles decreases sharply, resulting in the reduced structural strength of the soil. The soil breaks more completely

under external pressure, which leads to a change in both the collapsibility coefficient and the unconfined compressive strength.

4.2. Microstructure Parameter Analysis

Although SEM images can show the differences between different CLS contents in improved loess microscopic morphology and other aspects, it is difficult to quantitatively characterize indicators such as apparent pore ratio, probability entropy, fractal dimension value of porosity, and the relationship between microstructure and macroscopic properties.

For this purpose, we used a particle (pore) and crack analysis system (PCAS) to quantify and analyzes the SEM images. First, the SEM images were automatically segmented by threshold and optimally adjusted, then the soil particles and pores in the images were marked as black and white, respectively, by a binarization process (Figure 13). Finally, the binarized images were identified and analyzed to quantify microstructural parameters [38].

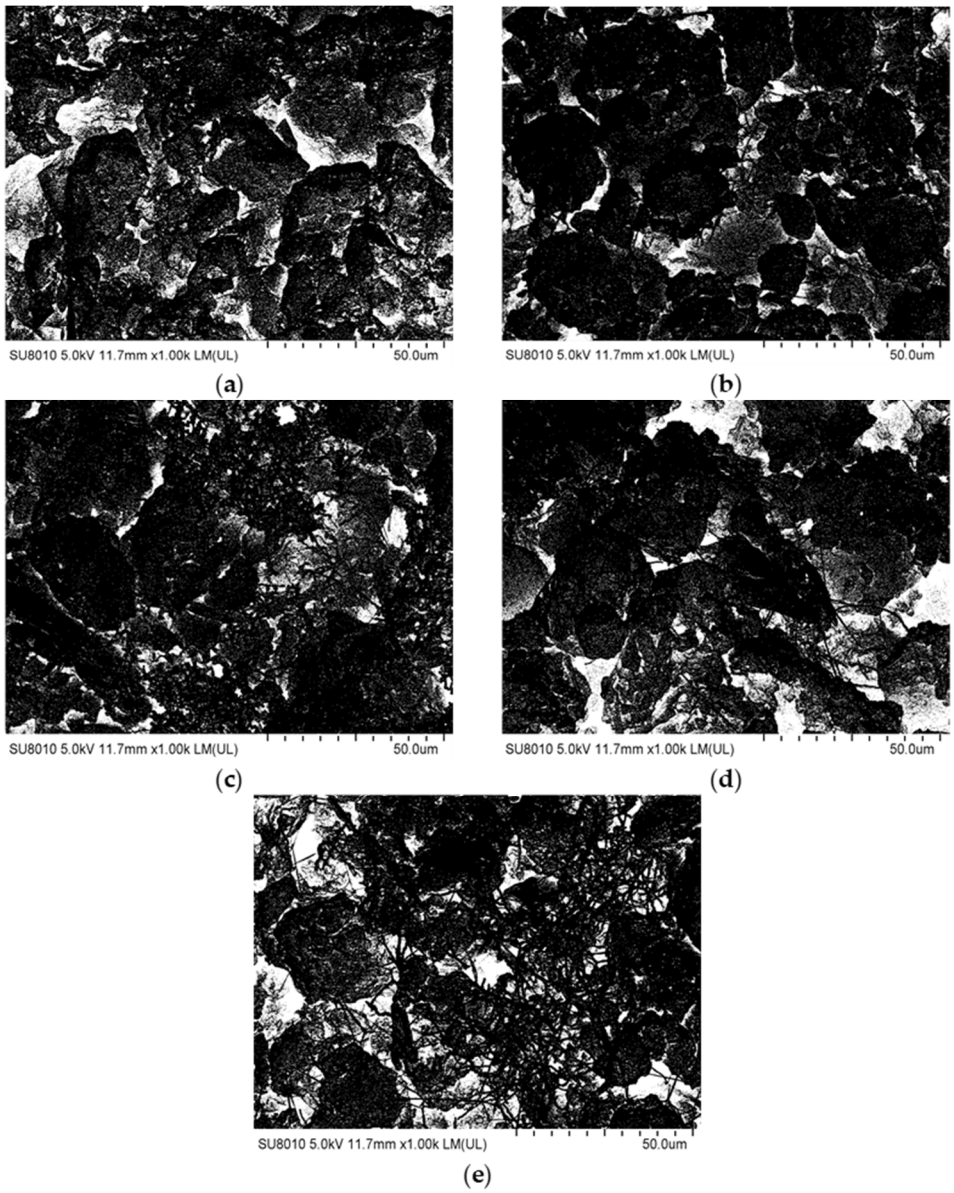

Figure 13. Binary image of improved loess with different CLS contents. (**a**) Binary image of untreated loess; (**b**) binary image of 1% CLS content; (**c**) binary image of 3% CLS content; (**d**) binary image of 5% CLS content; (**e**) binary image of 7% CLS content.

The apparent pore ratio is an essential indicator of soil dense degree. It is an indirect response to the various characteristics of the pore ratio in three-dimensional space using two-dimensional parameters. The apparent pore ratio can be characterized computationally by using the ratio of pore area to soil particle area in the binarized image [39]. The apparent pore ratio is calculated as follows:

$$N = \frac{A_p}{A_s} \tag{4}$$

where N is the apparent pore ratio, A_p is the area of pores in the SEM images (μm^2), and A_s is the area of soil particles in the SEM images (μm^2).

Figure 14 shows the apparent pore ratios of improved loess with different CLS content. As can be seen from the figure, with the increase in CLS content, the apparent pore ratio shows a trend of first decreasing and then increasing, and the lowest pore ratio is only 5.66% when the CLS content amount is 3%. As mentioned before, when the content is too high, CLS has an agglomeration effect, increasing the distance between soil particles and deteriorating the compactness of the soil [10].

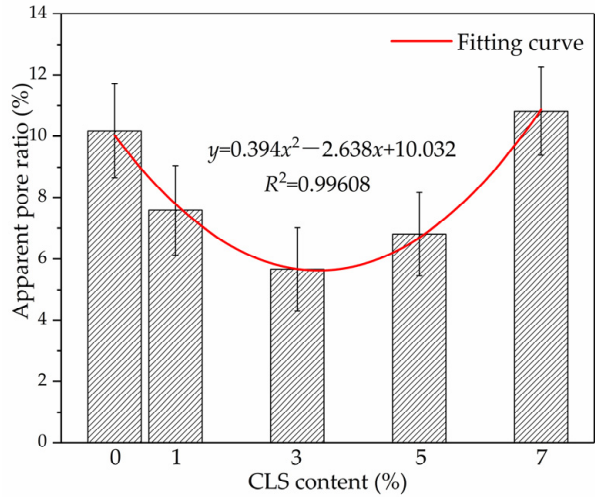

Figure 14. Apparent pore ratio of improved loess with different CLS content.

According to the results in Figure 14, the relationship between the content of CLS and the apparent pore ratio can be further fitted as:

$$\begin{gathered} y = 0.394x^2 - 2.638x + 10.032 \\ R^2 = 0.99608 \end{gathered} \tag{5}$$

Equation (5) shows that the relationship between CLS content and apparent pore ratio is a quadratic polynomial. From Equation (5), the apparent pore ratio was the lowest when the content of CLS was 3.35%, indicating that the improved loess had the densest state at this time, which is consistent with the macroscopic test results when the content of CLS was 3%.

Probability entropy is an index reflecting the degree of disorder of pore arrangements in soil. The smaller the probability entropy, the better the directionality and orderliness of pore arrangement [40]. The calculation formula is:

$$H_m = -\sum_{i=1}^{n} P_i \log_n P_i \tag{6}$$

where H_m is the probability entropy of the soil structure, taking values from 0 to 1, and P_i is the probability that the structural unit body is presented in a certain orientation zone.

Figure 15 shows the probability entropy of the improved loess with different CLS content. As seen from the figure, there is no apparent change in the probability entropy of

improved loess with different CLS content. However, the probability entropy was relatively high for untreated loess, relatively low at 3% and 5% CLS content, and slightly rebounding at 7% CLS content. This shows that the pore arrangement in the soil tends to be regularized under the coupling effect of CLS. This is consistent with the SEM results.

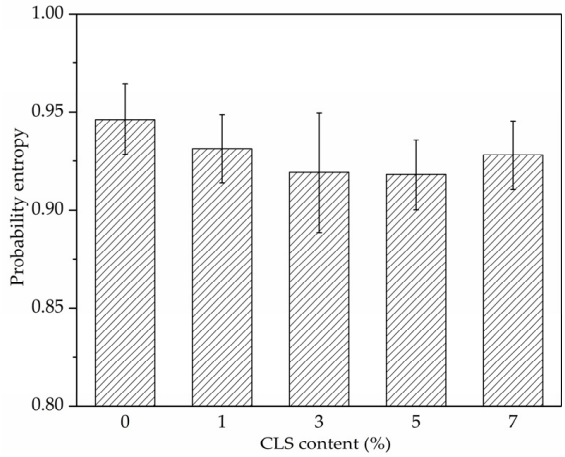

Figure 15. Probability entropy of improved loess with different CLS content.

The fractal dimension value of porosity is an index to characterize pore size distribution in the soil. The larger the fractional dimension value, the greater discrepancy in pore size in the soil. Its formula is [41]:

$$D_c = -\lim \frac{\ln N(r)}{\ln r} \tag{7}$$

where D_c is the fractal dimension value of porosity, r is the pore diameter (μm) and $N(r)$ is the number of pores larger than this pore diameter.

Figure 16 shows the fractal dimension value of the porosity of the improved loess with different CLS content. As seen from the figure, the fractal dimension value of porosity shows a trend of decreasing and then increasing after incorporating CLS. The minimum value of porosity fractional dimension at 3% CLS content indicates that the particle structure in the improved loess is more closely distributed at this time, and the pore size and arrangement pattern tend to be unified. Compared to untreated loess, although it is compacted, direct contact between soil particles leads to the existence of a large number of pores of different sizes [42]. Excessive CLS slightly reverses the porosity fractional dimension value due to weakening by the filling effect of the improved loess. However, the uniformity of the pore is still better than that of the untreated loess.

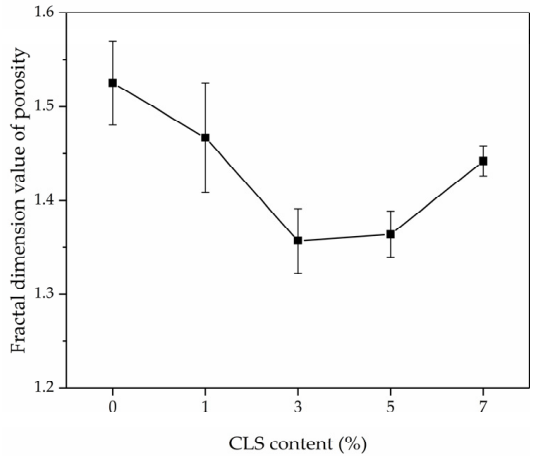

Figure 16. Fractal dimension value of porosity of improved loess with different CLS content.

4.3. X-ray Diffraction Test Analysis

SEM could only observe the changes in microscopic morphology before and after CLS modification. To clarify whether new minerals were formed before and after CLS modification, an XRD physical phase test analysis was conducted on untreated loess; 3% CLS improved soil at 28 d of age.

Figure 17 shows the XRD test results of the untreated loess and the improved loess. As can be seen from the figure, there was no apparent change in the mineral composition (quartz, dolomite, calcite, and albite) before and after the action of the modifier, and no obvious new mineral components were generated.

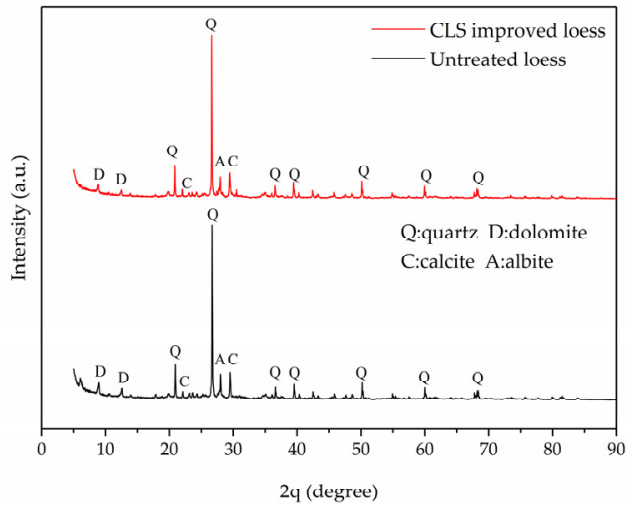

Figure 17. XRD analysis results.

It is important to note that although no new minerals were generated after the improvement with CLS, the mass fraction of each mineral component was changed, as shown in Table 5. It can be seen that the mass fractions of dolomite ($CaMg(CO_3)_2$) and calcite ($CaCO_3$) were increased to 28.7% and 12.6%, respectively, the mass fraction of quartz (SiO_2) was reduced to 38.1%, and the mass fraction of albite (Na Al Si_3O_8) remained unchanged, the reason being that Ca^{2+} ions in CLS reacted to form typical carbonate cementing materials such as ($CaMg(CO_3)_2$) and $CaCO_3$. The physical and mechanical properties of loess depend highly on the cementation and the degree of cementation in the soil. In contrast, carbonate cementation strength is higher than clay minerals, enhanced macroscopic properties.

Table 5. Mineral content of samples.

Sample	Quartz (%)	Dolomite (%)	Calcite (%)	Albite (%)
Untreated loess	43.3	24.6	11.8	20.4
CLS improved loess	38.1	28.7	12.6	20.6

To further investigate the strengthening mechanism of CLS-improved loess, the crystalline size of each mineral component before and after CLS improvement was calculated using the Scherrer equation as follows [43]:

$$L = \frac{\lambda k}{\beta \cos \theta} \tag{8}$$

where L is the crystalline size (nm), k is Scherrer constant (0.89 in this study), λ is the wavelength of X-radiation (1.540538 Å), and β is the width of a peak at half height expressed in 2θ (rad). Table 6 shows the grain size of each mineral fraction before and after CLS modification. It can be seen that the average grain size of each mineral composition was

reduced after the incorporation of CLS, and the degree of reduction was more than 50%. The decrease in grain size is closely related to the structural changes in the soil and the degree of cementation between minerals [44]. It is inferred that under the effect of ion exchange and protonation (Figure 18), the positive charge of CLS neutralizes the negative charge on the soil surface, thus reducing the thickness of the double layer and making the mineral composition more aggregated and denser [45].

Table 6. Grain size of mineral composition.

Mineral Types	Before Modification (nm)	After Modification (nm)	Decrement (%)
Quartz	371	185	50.13
Dolomite	301	123	59.14
Calcite	248	113	54.44
Albite	305	124	59.34

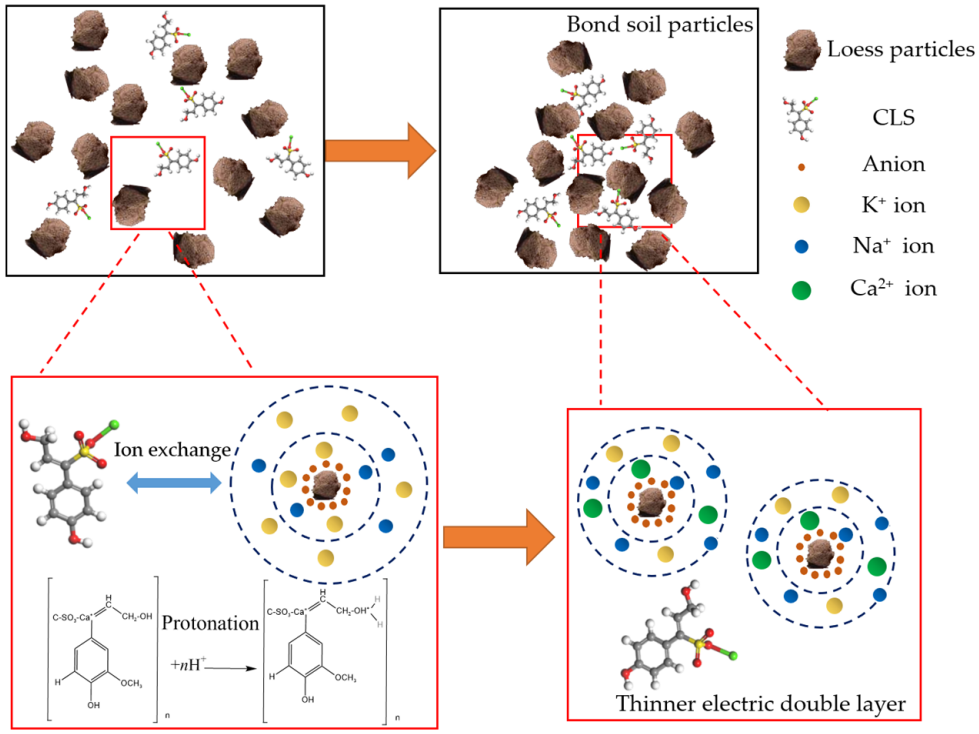

Figure 18. Schematic diagram of the mechanism of CLS improved loess.

These results are consistent with the findings of Zhang et al. [46]. and Vinod et al. [47] who also did not observe the generation of new compounds in the improved soils. They concluded that CLS adsorption occurs on the surface of clay minerals through electrostatic attraction. With time, CLS neutralizes the excess negative charges on the surface of the clay minerals, forming a bond with the clay particles. Finally, the CLS polymer chains pull the clay particles together to form aggregates or clusters of particles, that increase soil strength and resistance to collapsibility.

5. Conclusions

We investigated the influence of calcium lignosulfonate (CLS) on the collapsibility, gray correlation, unconfined compressive strength, and strengthening mechanism of loess in northwest China. The following conclusions are highlighted:

(1) CLS contains lipophilic groups such as phenyl propane, which can effectively inhibit water erosion. In this paper, the best content of CLS used to improve loess was 3%. Under a standard pressure of 200 kPa, the collapsibility coefficients were reduced by

more than 95% measured by single and double-oedometer methods. The collapsibility coefficient was positively correlated with the pore ratio and negatively associated with dry density and moisture content.

(2) A combination of physical quantities, such as substance composition and structural characteristics, determines loess collapsibility. According to grey correlation analysis, the physical indexes closely related to the collapsibility coefficient of loess were water content, void ratio, dry density, and CLS content, in turn. Although the content of CLS was smallest, its gray correlation was still more than 0.5, showing a significant correlation, and the ability to reduce the collapsibility of loess.

(3) Unconfined compressive strength continued to improve with the extension of curing age, with rapid strength growth during the first 14 d. The UCS of improved soil had a quadratic polynomial relationship with the content of CLS, and the maximum value was obtained at about 3%. When the content was too high, CLS agglomerated and reduced soil strength.

(4) CLS made the improved loess dense and stable by filling pores, linking soil particles, changing the connection between soil particles and the type of pores. By microstructural parameter analysis, the apparent pore ratio and CLS content showed a quadratic polynomial relationship. The probability entropy and fractal dimension values decreased first and then increased with the content of CLS.

(5) No new mineral components were formed in the improved soil, but the carbonate cements, such as Ca Mg $(CO_3)_2$ and $CaCO_3$, could strengthen soil structure. Under the action of protonation and ion exchange, the thickness of the double electric layer was reduced, and the grain size of each mineral was decreased by more than 50%, making the mineral composition denser.

WE have shown that CLS has the potential to stabilize loess against collapsible erosion. A solution to the problem of preventing the collapse of loess foundations and superstructures is provided. Soils improved by CLS will benefit sustainable infrastructure development compared to conventional modified additives. However, more chemical analysis is required to investigate the enhancement mechanism.

Author Contributions: Conceptualization, D.Z. and J.L.; methodology, Z.B.; validation, D.L., D.Z. and W.L.; formal analysis, Z.B.; investigation, Z.B.; resources, D.L. and W.L.; writing—original draft preparation, Z.B.; writing—review and editing, D.L. All authors have read and agreed to the published version of the manuscript.

Funding: This work was supported by the General program of the National Natural Science Foundation of China (51878547); National Natural Science Foundation of China Youth Science Fund (52008332); China Postdoctoral Fund Regional Special Support Program (2021M693877); Independent Research and Development project of State Key Laboratory of Green Building in Western China (LSZZ202225).

Institutional Review Board Statement: Not applicable.

Informed Consent Statement: Not applicable.

Data Availability Statement: All data generated or analyzed during this study are included in this published article.

Conflicts of Interest: The authors declare that they have no known competing financial interests or personal relationships that could have appeared to influence the work reported in this paper references.

References

1. Luo, H.; Wu, F.; Chang, J.; Xu, J. Microstructural constraints on geotechnical properties of Malan Loess: A case study from Zhaojiaan landslide in Shaanxi province, China. *Eng. Geol.* **2018**, *236*, 60–69. [CrossRef]
2. Xu, L.; Coop, M.R.; Zhang, M.; Wang, G. The mechanics of a saturated silty loess and implications for landslides. *Eng. Geol.* **2018**, *236*, 29–42. [CrossRef]

3. Peng, J.; Wang, G.; Wang, Q.; Zhang, F. Shear wave velocity imaging of landslide debris deposited on an erodible bed and possible movement mechanism for a loess landslide in Jingyang, Xi'an, China. *Landslides* **2017**, *14*, 1503–1512. [CrossRef]
4. Feng, S.; Du, F.; Shi, Z.; Shui, W.; Tan, K. Field study on the reinforcement of collapsible loess using dynamic compaction. *Eng. Geol.* **2015**, *185*, 105–115. [CrossRef]
5. Peng, L.; Wang, D.; Qi, J. Study on anti-corrosion of PVA-treated wheat straw and its application in reinforcement of a silty soil. *Constr. Build. Mater.* **2021**, *291*, 123305. [CrossRef]
6. Wang, F.; Li, K.; Liu, Y. Optimal water-cement ratio of cement-stabilized soil. *Constr. Build. Mater.* **2022**, *320*, 126211. [CrossRef]
7. Tabarsa, A.; Latifi, N.; Meehan, C.L.; Manahiloh, K.N. Laboratory investigation and field evaluation of loess improvement using nanoclay—A sustainable material for construction. *Constr. Build. Mater.* **2018**, *158*, 454–463. [CrossRef]
8. Ralph, J.; Lapierre, C.; Boerjan, W. Lignin structure and its engineering. *Curr. Opin. Biotechnol.* **2019**, *56*, 240–249. [CrossRef]
9. Park, G.W.; Gong, G.; Joo, J.C.; Song, J.; Lee, J.; Lee, J.-P.; Kim, H.T.; Ryu, M.H.; Sirohi, R.; Zhuang, X.; et al. Recent progress and challenges in biological degradation and biotechnological valorization of lignin as an emerging source of bioenergy: A state-of-the-art review. *Renew. Sustain. Energy Rev.* **2022**, *157*, 112025. [CrossRef]
10. Zhang, T.; Cai, G.; Liu, S. Assessment of mechanical properties in recycled lignin-stabilized silty soil as base fill material. *J. Clean. Prod.* **2018**, *172*, 1788–1799. [CrossRef]
11. Yang, B.; Zhang, Y.; Ceylan, H.; Kim, S.; Gopalakrishnan, K. Assessment of soils stabilized with lignin-based by-products. *Transp. Geotech.* **2018**, *17*, 122–132. [CrossRef]
12. Ceylan, H.; Gopalakrishnan, K.; Kim, S. Soil Stabilization with Bioenergy Coproduct. *Transp. Res. Rec. J. Transp. Res. Board* **2010**, *2186*, 130–137. [CrossRef]
13. Wang, Q.; Zhong, X.; Ma, H.; Wang, S.; Liu, Z.; Guo, P. Microstructure and reinforcement mechanism of lignin-modified loess. *J. Mater. Civ. Eng.* **2020**, *32*, 04020319. [CrossRef]
14. He, Z.; Fan, H.; Wang, J.; Liu, G.; Wang, Z.; Yu, J. Experimental study of engineering properties of loess reinforced by lignosulfonate. *Rock Soil Mech.* **2017**, *38*, 731–739. [CrossRef]
15. Hou, X.; Ma, W.; Li, G.; Mu, Y.; Zhou, Z.; Wang, F. Influence of lignosulfonate on mechanical properties of Lanzhou loess. *Rock Soil Mech.* **2017**, *38*, 18–26. [CrossRef]
16. *ASTM D4318-10*; Standard Test Methods for Liquid Limit, Plastic Limit, and Plasticity Index of Soils. ASTM: West Conshohocken, PA, USA, 2010.
17. *ASTM D698*; Standard Test Methods for Laboratory Compaction Characteristics of Soil Using Standard Effort. ASTM: West Conshohocken, PA, USA, 2012.
18. *GB50025-2018*; Building Specification of Collapsible Loess Region. China Architecture and Building Press: Beijing, China, 2018.
19. *ASTM D4219-02*; Test Method for Unconfined Compressive Strength Index of Chemical-Grouted Soils. ASTM: West Conshohocken, PA, USA, 2002.
20. Li, X.; Li, L.; Song, Y.; Hong, B.; Wang, L.; Sun, J. Characterization of the mechanisms underlying loess collapsibility for land-creation project in Shaanxi Province, China—A study from a micro perspective. *Eng. Geol.* **2019**, *249*, 77–88. [CrossRef]
21. Gao, C.; Du, G.; Liu, S.; Zhang, D.; Zhang, K.; Zeng, B. Field study on the treatment of collapsible loess using vibratory probe compaction method. *Eng. Geol.* **2020**, *274*, 105715. [CrossRef]
22. Chen, Q.; Indraratna, B.; Carter, J.; Rujikiatkamjorn, C. A theoretical and experimental study on the behaviour of lignosulfonate-treated sandy silt. *Comput. Geotech.* **2014**, *61*, 316–327. [CrossRef]
23. Kuo, Y.; Yang, T.; Huang, G. The use of grey relational analysis in solving multiple attribute decision-making problems. *Comput. Ind. Eng.* **2008**, *55*, 80–93. [CrossRef]
24. Deng, J. Control problems of grey systems. *Syst. Control Lett.* **1982**, *1*, 288–294. [CrossRef]
25. Ren, S.; Wang, C.; Xiao, Y.; Deng, J.; Tian, Y.; Song, J.; Cheng, X.; Sun, G. Thermal properties of coal during low temperature oxidation using a grey correlation method. *Fuel* **2020**, *260*, 116287. [CrossRef]
26. Wu, F.; Xu, W.; Zhang, F.; Wu, H. Grey correlation analysis of physical properties and evaluation index of graphene-oxide-modified asphalt. *Coatings* **2022**, *12*, 770. [CrossRef]
27. Zhu, C.; Luo, H.; Tian, W.; Teng, B.; Qian, Y.; Ai, H.; Xiao, B. Investigation on fatigue performance of diatomite/basalt fiber composite modified asphalt mixture. *Polymers* **2022**, *14*, 414. [CrossRef]
28. Wu, X.; Zhao, Y.; Xu, A.; Mi, W.; Zhao, S. Correlation of collapsibility of loess with physical indexes and evaluation methods. *J. Yangtze River Sci. Res. Inst.* **2018**, *35*, 75–80. [CrossRef]
29. Cai, G.; Zhang, T.; Liu, S.; Li, J.; Jie, D. Stabilization mechanism and effect evaluation of stabilized silt with lignin based on laboratory data. *Mar. Georesour. Geotechnol.* **2016**, *34*, 331–340. [CrossRef]
30. Zhang, T.; Liu, S.; Cai, G.; Puppala, A.J. Experimental investigation of thermal and mechanical properties of lignin treated silt. *Eng. Geol.* **2015**, *196*, 1–11. [CrossRef]
31. Wang, F.; Shi, H.; Huang, L.; Zhou, L.; Li, J.; Zeng, M.; Cao, Y.; Lai, D. The technical system of biological measure on controlling of water and soil loss in hilly region of red earth. *Res. Soil Water Conserv.* **2005**, *12*, 248–251.
32. Kong, X.; Wang, G.; Liang, Y.; Zhang, Z.; Cui, S. The engineering properties and microscopic characteristics of high-liquid-limit soil improved with lignin. *Coatings* **2022**, *12*, 268. [CrossRef]
33. Zhang, T.; Yang, Y.L.; Liu, S.Y. Application of biomass by-product lignin stabilized soils as sustainable Geomaterials: A review. *Sci. Total Environ.* **2020**, *728*, 138830. [CrossRef]

34. Ceylan, H.; Kim, S.; Gopalakrishnan, K. *Sustainable Utilization of Bio-Fuel Co-Product in Roadbed Stabilization*; Springer: London, UK, 2012; pp. 117–129.
35. Ji, Y.; Ma, Q.; Li, X.; Tian, Y.; Cao, P. Study on composite improvement of silt sites by lignin and sodium methylsilicate and its micro mechanism. *Coatings* **2022**, *12*, 1647. [CrossRef]
36. Liu, Z.; Liu, F.; Ma, F.; Wang, M.; Bai, X.; Zheng, Y.; Yin, H.; Zhang, G. Collapsibility, composition, and microstructure of loess in China. *Can. Geotech. J.* **2016**, *53*, 673–686. [CrossRef]
37. Sun, Y.; Tang, L. Use of X-ray computed tomography to study structures and particle contacts of granite residual soil. *J. Cent. South Univ.* **2019**, *26*, 938–954. [CrossRef]
38. Liu, C.; Tang, C.; Shi, B.; Suo, W. Automatic quantification of crack patterns by image processing. *Comput. Geosci.* **2013**, *57*, 77–80. [CrossRef]
39. Gundogar, A.; Ross, C.; Akin, S.; Kovscek, A. Multiscale pore structure characterization of Middle East carbonates. *J. Pet. Sci. Eng.* **2016**, *146*, 570–583. [CrossRef]
40. Brus, D.J.; Bogaert, P.; Heuvelink, G.B.M. Bayesian maximum entropy prediction of soil categories using a traditional soil map as soft information. *Eur. J. Soil Sci.* **2008**, *59*, 166–177. [CrossRef]
41. Liu, Y.; Chen, L.; Wang, H.; Jiang, L.; Zhang, Y.; Zhao, J.; Wang, D.; Zhao, Y.; Song, Y. An improved differential box-counting method to estimate fractal dimensions of gray-level images. *J. Vis. Commun. Image Represent.* **2014**, *25*, 1102–1111. [CrossRef]
42. Tang, C.; Lin, L.; Cheng, Q.; Zhu, C.; Wang, D.; Lin, Z.; Shi, B. Quantification and characterizing of soil microstructure features by image processing technique. *Comput. Geotech.* **2020**, *128*, 103817. [CrossRef]
43. Drits, V.; Środoń, J.; Eberl, D. XRD measurement of mean crystallite thickness of illite and illite/smectite: Reappraisal of the Kubler index and the Scherrer equation. *Clays Clay Miner.* **1997**, *45*, 461–475. [CrossRef]
44. Alazigha, D.P.; Indraratna, B.; Vinod, J.S.; Heitor, A. Mechanisms of stabilization of expansive soil with lignosulfonate admixture. *Transp. Geotech.* **2018**, *14*, 81–92. [CrossRef]
45. Zhong, X.; Liang, Y.; Wang, Q.; Ma, J.; Liang, S.; Wang, Y.; Xu, X. Evaluation and analysis of the effect of lignin amelioration on loess collapsibility. *J. Renew. Mater.* **2022**, *10*, 3405–3424. [CrossRef]
46. Zhang, T.; Cai, G.; Liu, S. Application of lignin-stabilized silty soil in highway subgrade: A macroscale laboratory study. *J. Mater. Civ. Eng.* **2018**, *30*, 04018034. [CrossRef]
47. Vinod, J.S.; Indraratna, B.; Mahamud, M.A.A. Stabilisation of an erodible soil using a chemical admixture. *Proc. Inst. Civ. Eng. Ground Improv.* **2010**, *163*, 43–51. [CrossRef]

Disclaimer/Publisher's Note: The statements, opinions and data contained in all publications are solely those of the individual author(s) and contributor(s) and not of MDPI and/or the editor(s). MDPI and/or the editor(s) disclaim responsibility for any injury to people or property resulting from any ideas, methods, instructions or products referred to in the content.